Dislocation creep near the frictional-viscous transition in blueschist: experimental constraints

Lonnie J. Hufford [1], Leif Tokle [1], Whitney M. Behr [1], Luiz F. G. Morales [1,2], and Claudio Madonna [1]

[1]Structural Geology and Tectonics Group, Geological Institute, Department of Earth Sciences, ETH Zürich, Zürich, Switzerland
[2]Scientific Center for Optical and Electron Microscopy (ScopeM), ETH Zürich, Otto-Stern-Weg 3, 8093, Zürich, Switzerland

Correspondence: Lonnie J. Hufford (lonnie.hufford@erdw.ethz.ch)

Abstract. Mafic oceanic crustal rocks at blueschist facies conditions are an important rheological component of subducting slabs and the interface at subduction plate boundaries. However, the mechanical properties and deformation mechanisms of glaucophane, a rheologically-controlling sodic amphibole in blueschists, are poorly constrained. To investigate its mechanical and microstructural properties, we conducted general shear constant rate

5 and strain rate stepping experiments on glaucophane aggregates using a Griggs apparatus at temperatures of 700-750°C, shear strain rates of $\sim 3 \times 10^{-6}$ to $9 \times 10^{-5} \mathrm{s}^{-1}$, varying grain sizes, and a confining pressure of $\sim$1.0 GPa. The constant rate experiments show an initial stage of grain-size-dependent strain hardening followed by weakening associated with brittle slip along cleavage planes, kink-band development, cataclasis resulting in a fine-grained matrix, and dislocation glide. These experiments evolved to a steady-state stress that did not depend on starting

10 grain size, showing evidence for subgrain development and dynamic recrystallization by bulge nucleation, interpreted to reflect dislocation creep with limited recovery by climb. The mechanical behavior and microstructures of glaucophane in our experiments are consistent with experiments on other low-symmetry minerals as well as microstructural observations from natural blueschists. The strain rate stepping experiments were used to develop a dislocation creep flow law for glaucophane with values of $A = 2.23 \times 10^5$ MPa^{-n} s^{-1}, $n = 3$, and $Q = 341 \pm$

15 37 kJ/mol. A deformation mechanism map comparing our dislocation creep flow law to an existing flow law for blueschist diffusion creep indicates dislocation creep should activate at lower temperatures, higher stresses and larger diffusion lengthscales. Viscosities predicted by our flow law for a typical subduction strain rate of 1×10^{-12} s^{-1} lie between quartz and eclogite dislocation creep for the blueschist stability field, implying that mafic oceanic crustal rocks remain strong relative to quartz-rich metasediments all along the subduction interface.

1 INTRODUCTION

Mafic oceanic crustal rocks that occupy the top several kilometers of subducting oceanic lithosphere exert an important influence on the rheology, stress distributions, and earthquake potential of the subduction interface (Wang and Bilek, 2011; Sun et al., 2020; Braden and Behr, 2021). As mafic oceanic crust is subducted, it enters the blueschist facies and undergoes important mineralogical changes, marked by abundant growth of sodic amphibole, along with possible lawsonite, epidote, white mica, quartz and other accessory phases (Evans, 1990). Despite that blueschist facies mafic rocks occupy a large portion of the downgoing slab and the subduction interface itself, the rheological properties of blueschists remain poorly characterized. Observations from the rock record provide some clues on the rheology of mafic blueschists relative to other potential subduction inputs. For example, blueschists are commonly found as lenses or boudins within metasedimentary or serpentinite-matrix mélanges (e.g. Liou et al., 1975; Cowan, 1978; Hefferan et al., 2002; Ernst, 2016), while in mafic-dominated terranes metamorphosed to eclogite facies, blueschists tend to form the matrix surrounding stronger eclogite blocks (Davis and Whitney, 2006; Cao et al., 2013; Kotowski and Behr, 2019). These observations suggest a qualitative rheological heirarchy in which the strength of mafic blueschists is intermediate between metasedimentary rocks and eclogite, but more quantitative constraints on the mechanisms controlling blueschist deformation are needed.

Microstructural observations from naturally and experimentally deformed sodic amphibole, as the primary rheologically-controlling mineral in blueschists, suggest that a wide range of deformation mechanisms are possible, ranging from brittle/frictional creep, to grain size sensitive and insensitive crystal-plastic (viscous) deformation mechanisms. Several studies, for example, suggest that sodic amphibole deforms via dislocation mechanisms such as dislocation glide or creep, based on the presence of undulose extinction, subgrain development, and/or dynamic recrystallization (Reynard et al., 1989; Kim et al., 2013; Cao et al., 2013; Kim et al., 2015; Behr et al., 2018; Kotowski and Behr, 2019). Other studies discuss evidence for dissolution-precipitation creep processes based on the presence of micro-boudinage with new amphibole growth in boudin necks, or new amphibole overgrowths oriented parallel to the foliation (Misch, 1969; Tokle et al., 2023a; De Caroli et al., 2024). Some studies have also documented brittle deformation and cataclasis (Ildefonse et al., 1990; Muñoz-Montecinos et al., 2023). Despite these insights, an experimental framework to systematically quantify the influence of key variables such as temperature, pressure, strain rate, and grain size, on these deformation processes has not yet been established.

Previous experimental work on sodic amphibole has focused on its bulk modulus (Jenkins et al., 2010), development of crystallographic preferred orientations (CPO) (Park et al., 2020; Park and Jung, 2022), its seismic velocity and anisotropy (Ha et al., 2019; Park and Jung, 2022), and the role of dehydration embrittlement (Kim et al., 2015; Incel et al., 2017). Tokle et al. (2023a) provided the first flow law for mafic polymineralic blueschists, describing conditions under which they deform via diffusion creep associated with microboudinage. In this paper, we build on these existing experimental constraints by focusing on the mechanical and microstructural properties of sodic amphibole (glaucophane) aggregates. We present a suite of general shear deformation experiments conducted using

55 a Griggs apparatus in which we varied temperature (700-750°C), shear strain rate ($\sim 3.0\mathrm{x}10^{-6}$/s to $\sim 9.6\mathrm{x}10^{-5}$/s), and starting grain size (<63 μm, 75-90 μm, and 63-355 μm). Based on our mechanical and microstructural results we demonstrate that glaucophane deforms by kinking, slip on cleavage planes, and fracturing during early work hardening, before switching to a dislocation-dominated deformation mechanism at mechanical steady state. Integrating the mechanical and microstructural data, we develop a flow law that can approximate the strength of

60 sodic-amphibole-rich blueschist and we discuss the larger-scale implications for oceanic crustal deformation in subduction zones.

2   METHODS

2.1   Starting Material

The starting material for our experiments is derived from a MORB blueschist from the Cycladic Blueschist Unit on
65 Syros island, Greece (same locality as described in Behr et al. (2018)). The original rock consisted of glaucophane, garnet, white mica, epidote, omphacite, and titanite (Fig. S.1). Through a series of mineral separation techniques including SELFrag rock crushing, sieving, Wilfley water table separation, magnetic separation, heavy liquid separation, and hand-picking, we obtained powders with >98% glaucophane. From this powder, we defined three grain size distributions for the experiments: a coarse-grained distributed fraction of 63-355 μm, a medium-grained
70 narrower fraction of 75-90 μm, and a third grain size fraction produced by crushing large glaucophane grains in a mortar and pestle to produce a fine-grained powder measured with EBSD data (<63 μm) (Fig. S.2).

2.2   Experimental Procedures

All experiments were performed with a Griggs apparatus in the Rock Physics and Mechanics laboratory at ETH Zürich. The experiments used a solid salt (NaCl) assembly and were conducted "as-is" (without pre-drying or
75 adding water to the sample). We used annealed Pt jackets that were lined with a 25 μm thick Ni foil, where glaucophane powder was placed between two grooved alumina (Al_2O_3) pistons cut at 45°. Both ends of the Pt jacket were welded shut with Pt cups. Each experiment used a K-type thermocouple where the thermocouple was oriented perpendicular to the shear direction.

The experiments included three hydrostatic, five constant rate, and three strain-rate-stepping, all at a confining
80 pressure of ~ 1.0 GPa. The hydrostatic experiments were brought to and kept at 700°C and 1.0 GPa for ~ 24-88 hours. These were used to determine the starting sample thickness for processing the mechanical data, the starting grain size after compaction and pressurization, and the initial microstructures prior to deformation. Three constant rate experiments were conducted on the medium grain size fraction at 700°C and a shear strain rate of $\sim 3.4\times10^{-6}\mathrm{s}^{-1}$ to examine the mechanical and microstructural evolution of the samples with increasing strain— these were quenched
85 at peak stress, during strain weakening, and at mechanical steady state. Two additional constant rate experiments

were conducted at the same conditions, but using different grain size fractions, to assess the role of grain size. See supplemental material for additional information on amphibole composition and stability (Fig. S.3).

Strain rate stepping experiments were carried out at 700°C, 725°C, and 750°C with four to six strain rate steps and shear strain rates ranging from $\sim 4.0 \times 10^{-6} \text{s}^{-1}$ to $\sim 9.6 \times 10^{-5} \text{s}^{-1}$. Following previous studies (e.g. Getsinger and Hirth, 2014; Proctor and Hirth, 2016; Okazaki and Hirth, 2020), the σ_1 motor rate was stepped for one 700°C experiment during the Pb run-in prior to deforming the sample to estimate the rate-dependence on internal friction, where the precision of the stress measurement at our deformation conditions is ± 8 MPa (Table S.1; Fig. S.4). At the end of each experiment, samples were quenched to preserve the microstructures, with the temperature lowered to 200°C at a rate of 4°C/s. During decompression, σ_1 was kept several hundred megapascals above σ_3 to avoid decompression cracking. After the experiments, the samples were cut in half perpendicular to the shear plane where one half was used for thin sectioning.

2.3 Data Processing

Force data were collected by an external load cell on the Griggs apparatus and recorded at a sampling rate of 1 Hz. A modified version of the open source code RIG (https://mpec.scripts.mit.edu/peclab/software/) for the ETH Zürich Griggs apparatus was used to process the mechanical data. Raw data are down-sampled and a median filter is applied to reduce electrical noise. All deformation experiments were corrected for sample thinning and area correction with the exception of the peak stress sample where no area correction is applied. Mechanical data for all experiments can be found in Table 1 and data without the Pb corrections can be found in Table S.2.

Table 1. Summary of Experiments

Sample ID	Shear Stress (MPa)	Equivalent Stress (MPa)	Shear Strain Rate (s^{-1})	Equivalent Strain Rate (s^{-1})	Shear Strain (γ)	Peak Shear Stress (MPa)	T (°C)	P (GPa)	Time at T & P for Hydrostatic (hr)	Grain Size (μm)
LH037	-	-	-	-	-	-	700	0.99	37	Coarse: 63-355
LH042a	192	384	9.3×10^{-6}	5.4×10^{-6}	1.36	469	700	1.06	-	Coarse: 63-355
b	271	544	3.4×10^{-5}	2.0×10^{-5}	2.64	-	700	1.07	-	-
c	232	465	2.4×10^{-5}	1.4×10^{-5}	3.28	-	700	1.08	-	-
d	186	372	1.2×10^{-5}	6.9×10^{-6}	3.57	-	700	1.08	-	-
e	156	310	6.9×10^{-6}	4.0×10^{-6}	3.76	-	700	1.08	-	-
f	145	285	4.0×10^{-6}	2.3×10^{-6}	3.93	-	700	1.08	-	-
LH045a	142	284	3.7×10^{-5}	2.1×10^{-5}	1.06	360	750	1.07	-	Coarse: 63-355
b	189	379	9.6×10^{-5}	5.5×10^{-5}	2.31	-	750	1.08	-	-
c	57	107	4.7×10^{-6}	2.7×10^{-6}	2.61	-	750	1.08	-	-
d	117	230	2.0×10^{-5}	1.2×10^{-5}	3.04	-	750	1.08	-	-
LH049	177	354	3.3×10^{-6}	1.9×10^{-6}	1.92	393	700	1.08	-	Coarse: 63-355
LH060	-	-	-	-	-	-	700	1.03	88	Medium: 75-90
LH062	158	316	3.4×10^{-6}	2.0×10^{-6}	1.96	283	700	1.06	-	Medium: 75-90
LH070*	191	382	3.7×10^{-6}	2.1×10^{-6}	0.59	255	700	1.02	-	Medium: 75-90
LH071*	273	546	2.0×10^{-6}	1.2×10^{-6}	0.3	273	700	1.04	-	Medium: 75-90
LH079	171	342	3.0×10^{-6}	1.7×10^{-6}	1.76	226	700	1.04	-	Fine: <63
LH089	-	-	-	-	-	-	700	1.01	24	Fine: <63
LH095a	210	420	2.7×10^{-5}	1.6×10^{-5}	1.14	461	725	1.03	-	Medium: 75-90
b	268	537	6.7×10^{-5}	3.9×10^{-5}	2.29	-	725	1.03	-	-
c	134	264	1.2×10^{-5}	6.9×10^{-6}	2.84	-	725	1.04	-	-
d	327	655	6.3×10^{-5}	3.6×10^{-5}	3.61	-	725	1.04	-	-

2.4 Electron Backscatter Diffraction

105 Crystallographic data were collected using the electron backscatter diffraction (EBSD) technique in a scanning electron microscope (SEM). EBSD data for the medium- and coarse-grained fraction hydrostatic samples were collected with an EDAX camera while the other samples were measured in a Hitachi SU5000 FEG SEM with an Oxford Symmetry 2 EBSD camera and Aztec software in the Scientific Centre for Optical and Electron Microscopy (ScopeM) of ETH Zürich. Details on sample polishing (Table S.3) and run settings are provided in the supplementary material.

110 All EBSD maps from deformed samples were made in the central regions of the sample. Mis2mean maps show intragranular misorientations, calculated as the minimum rotation angle between the pixel orientation and the mean orientation of the grain (Chauve et al., 2017). All EBSD pole figures are plotted as one average point per grain.

3 RESULTS

3.1 Hydrostatic experiments

115 The hydrostatic experiments with different grain size fractions were used to characterize the microstructures of the starting material. All three grain size fractions exhibit a) crushing at grain margins, b) minor amounts of kinking and fracturing, c) weak shape preferred orientations (SPO), and d) moderate crystallographic preferred orientations (CPO) (Fig. 1). These deformation features occur without any microstructural evidence for amphibole breakdown (Fig. 1). The CPOs show strong maxima in the (110) and (100) orientations, a diffuse pattern in the (010) orientation,

120 and a weak girdle in the (001) orientation, consistent with rigid-body rotation during hot-pressing (Fig. 4). The amount of grain crushing observed in the hydrostatic samples correlates with the initial grain size fraction, with the smallest grain size fraction showing less than the largest grain size fraction (Fig. 1). The presence of fine grains along larger grain boundaries has been documented in previous studies and is common for powdered starting materials used for Griggs apparatus experiments (Tullis and Yund, 1985, 1987; Tokle et al., 2021, 2023b). See supplemental

125 material (Fig. S.5) for EBSD maps showing orientation and internal misorientation maps.

3.2 Strain Evolution Experiments

3.2.1 Mechanical Data

The mechanical data for the strain evolution experiments show good reproducibility, with peak stresses and weakening rates within error for the Griggs apparatus (Fig. 2a) (±30 MPa, Holyoke III and Kronenberg, 2010). For each

130 experiment, the peak stress was reached at a shear strain of ∼0.3 and a shear stress of ∼260 MPa. For the high strain experiment, this was followed by pronounced strain weakening over a strain increment of ∼0.4, culminating in an approximate mechanical steady state at a shear strain of ∼0.8 and remaining until the experiment was quenched
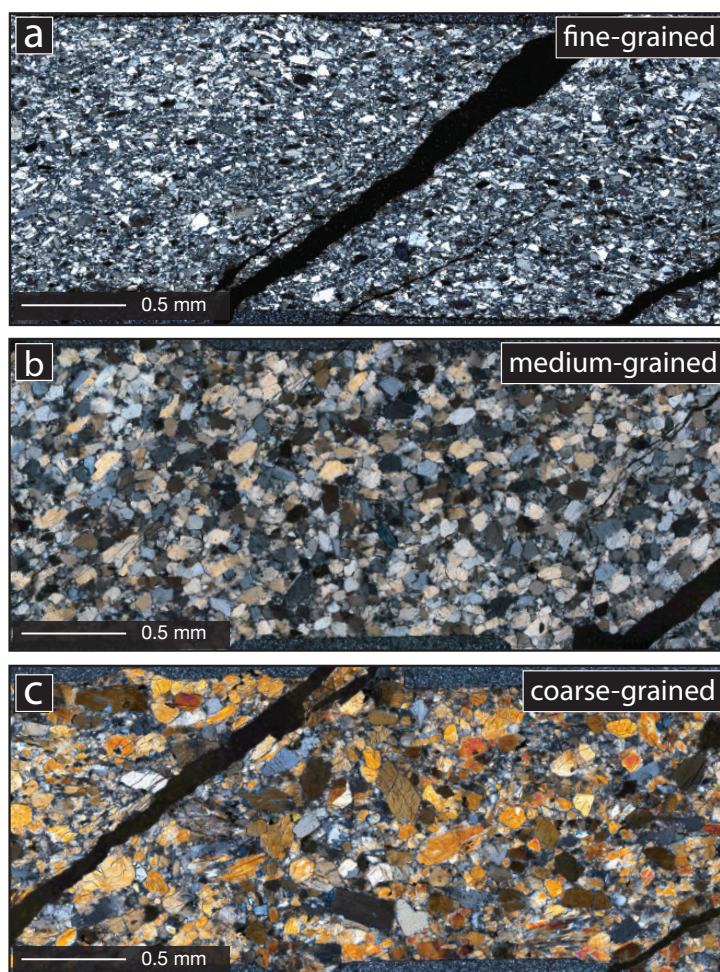
Figure 1. Starting material (hydrostatics) in three grain size fractions. a) fine-grained, b) medium-grained, and c) coarse-grained. All photomicrographs are taken in cross-polarized light with the alumina shear pistons at the bottom and top of each sample. Black spaces at 45° are the result of decompression cracking.

at a shear strain of ~2.0. In this experiment the sample weakened ~44% from a peak stress of 283 MPa to a steady state stress of 158 MPa (Fig. 2a).

135 ### 3.2.2 Microstructures

Peak Stress. The peak stress sample macroscopically resembles the hydrostatic experiment for the same grain size, showing no foliation (Fig. 3a). In detail, however, there are several differences compared to the hydrostatic experiment including the following: 1) Most grains show undulose extinction (Fig. 3d, pink arrow). 2) Fractures are more prominent and are oriented both along and oblique to amphibole cleavages. 3) Grain size reduction of

140 relict grains produced small angular grains (composing ≥5%) down to 10 μm in diameter, especially along cleavage planes and kink bands (Fig. 3d, pink arrow) 4) There are pull-apart structures visible in several grains, in which both extensional and shear motion are concentrated along fractures and kink bands (Fig. 3a,d). The EBSD map in Figure 5a shows examples of fractured and kinked relict grains with angular finer-grained comminuted zones along their margins and within dilational fracture zones. The mis2mean map in Figure 5d shows that the relict

145 grains exhibit weak undulose extinction in places, but sharp angular fracture zones with local comminution and sharp misorientations are much more common. The CPOs in this sample display maxima perpendicular to the shear plane in the (110) and (100) plots, a less diffuse (010) maxima/girdle in the (010) plot, and girdling parallel to the shear direction in the (001) plot.

Weakening. The strain weakening sample shows more fracturing, kinking, and undulose extinction as well as

150 a greater amount (≥10%) of fine-grained matrix compared to the peak stress sample (Fig. 3b). Similar to the peak stress sample, there is no foliation and many grains show kink bands with undulose extinction where slip along cleavage planes and kink bands result in pull-apart structures (Fig. 3b). The EBSD maps in Figure 5b show several relict grains with their surrounding matrix. The IPF-X map illustrates that several fine-grained clusters have similar crystallographic orientations to the relict grains they surround (Fig. 5b, white arrow). The mis2mean map shows

155 high degrees of misorientation and the development of subgrains within some relict grain interiors, e.g. along kink boundaries (Fig. 5e, white arrow) and cleavage-parallel fracture planes (Fig. 5b). The CPOs are similar to the peak stress CPOs, but the girdling of the (010) and (001) axes appears weaker, approaching point maxima in the shear plane perpendicular and parallel to the shear direction, respectively.

Mechanical Steady State. The steady state sample shows significantly more grain size reduction relative to the

160 peak stress and strain weakening samples, with ≥25% fine-grained material defining anastomosing shear zones throughout the sample (Fig. 3c). A moderate foliation parallel to the shear plane is developed and shear bands dipping shallowly in the shear direction (C' orientations) are also prominent (Fig. 3c,f). Some relict grains in this sample exhibit undulose exinction, kink bands and bookshelf-slip, but in several grains a more organized subgrain structure is observed with subgrains oriented perpendicular and parallel to the direction of shear (Figs. 5 and 6).

165 Internal misorientations and subgrain development in the relict grains tend to increase toward the grain margins, commonly culminating in clusters of new grains (similar to or smaller in size than the subgrains) (Fig.6). The
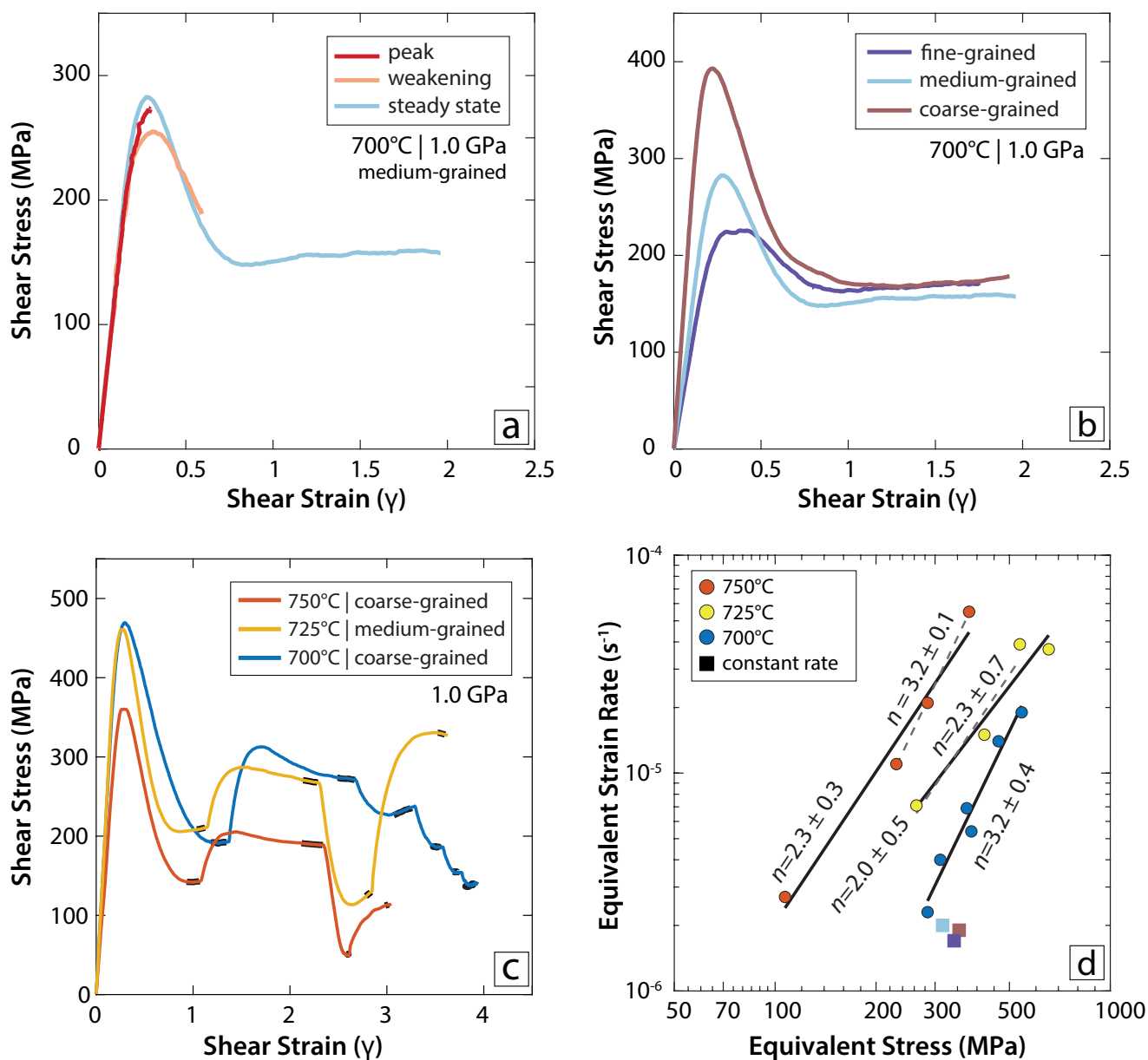
Figure 2. Mechanical data from constant rate (a and b) and strain rate stepping (c and d) experiments. a) Shear stress versus shear strain plot of the constant rate experiments at $700°C$ and 1.0 GPa at a shear strain rate of $\sim 3.4 \times 10^{-6}$/s at peak stress, weakening, and mechanical steady state. b) Shear stress versus shear strain plot of different grain size fractions deformed at similar conditions to a). c) Shear stress versus shear strain plot of the strain rate stepping experiments at $700°C$, $725°C$, and $750°C$ and 1.0 GPa. Areas highlighted in black indicate the regions of mechanical steady state. d) Stress exponents from the strain rate stepping experiments in (c) with constant rate experiments from (b) for comparison.
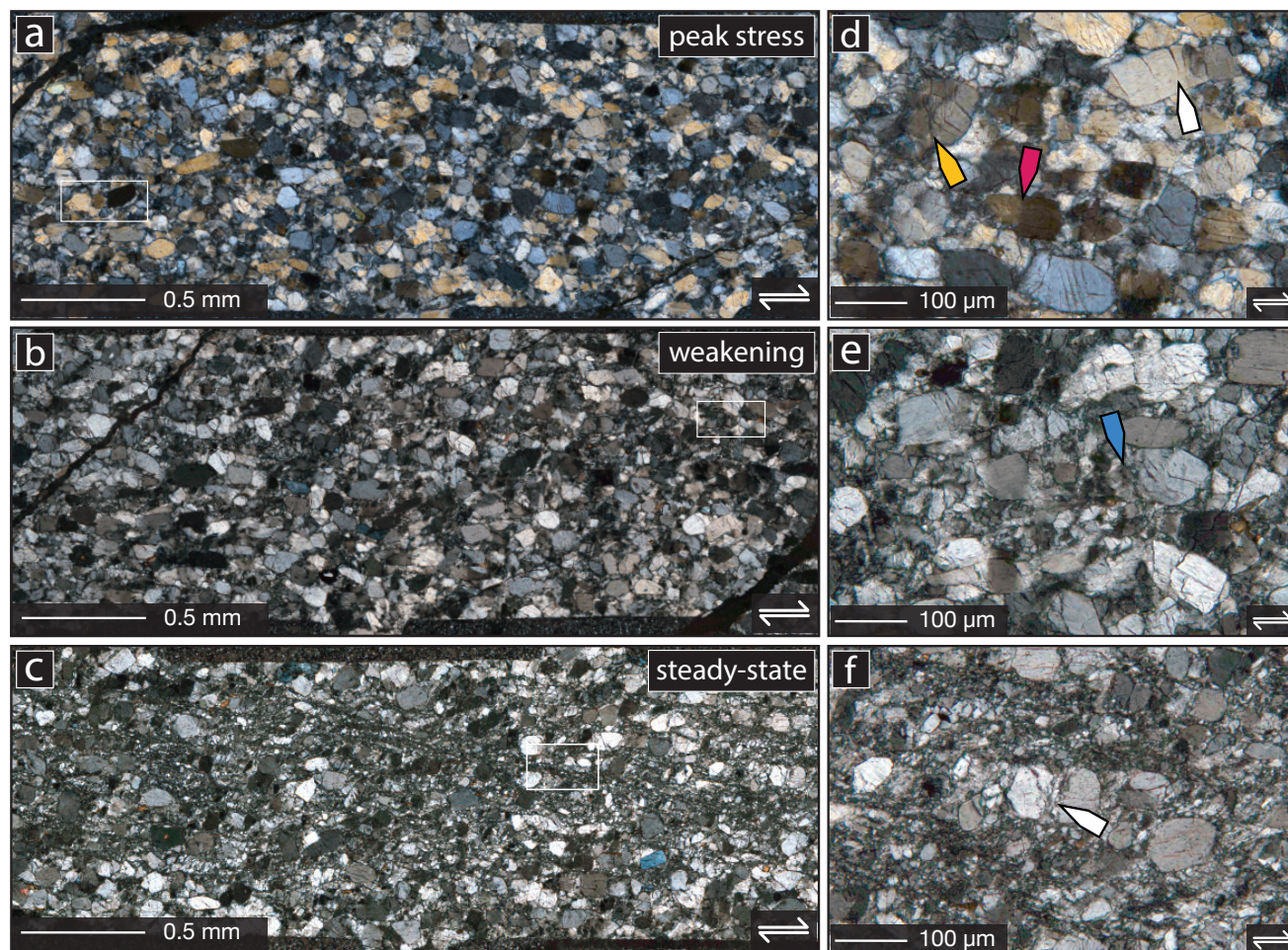
Figure 3. Photomicrographs of the medium-grained size fraction peak stress (a and d), weakening (b and e) and mechanical steady state samples (c and f). The white boxes highlight EBSD map locations. d) the white arrow shows intragranular fractures that terminate within grains, the yellow arrow shows intragranular fractures that span entire grains, and the pink arrow shows grains that are kinked with undulose extinction. e) the blue arrow shows pull apart structures localized at kink bands with comminuted grains in the kink bands. f) the white arrow shows finer grains in a pull apart structure neck. All photomicrographs taken with cross-polarized light and have a dextral shear sense.
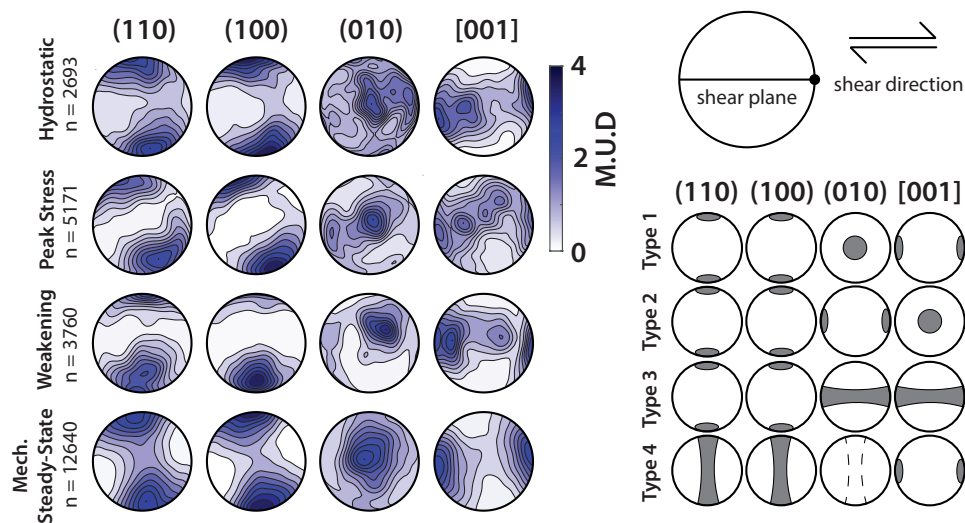
Figure 4. Pole figures from the medium-grained size fraction hydrostatic, peak stress, weakening, and mechanical steady state EBSD maps. Data are presented in multiples of uniform density (M.U.D) where each pole figure is scaled from 0 to 4. n represents the number of grains where a mean orientation of each grain was plotted. The pole figures are plotted in the kinematic reference frame with the x-direction consistent with the direction of shear. The CPO Types figure is modified after Kim and Jung, 2019, where the dashed lines in the (010) pole figure represents our interpretation of a Type 4 CPO.

orientation of subgrain boundaries are consistent with slip on multiple known slip systems in glaucophane (e.g., Reynard et al. (1989)) and supports activation of at least two slip systems, in addition to slip on {110} cleavage planes (Fig. 6). In the fine-grained shear zone domains, on average, grains show low degrees of internal misorientation

170 suggesting they are relatively strain-free (Fig. 6). In some places where grains with internal misorientation contrasts are juxtaposed, there are highly lobate grain boundaries consistent with grain boundary migration (Figs. 5,6). The mechanical steady state CPO shows differences compared to the peak stress and hydrostatic samples in that the (010) axis exhibits a point maxima, rather than a girdle, along the shear plane perpendicular to the shear direction, while simultaneously the (001) axis forms a point maxima parallel to the shear plane and the shear direction (Fig.

175 4).

3.3 Grain Size Fraction Experiments

3.3.1 Mechanical Data

The experiments conducted to steady-state conditions with different initial grain size fractions show a clear relationship between grain size and peak stress, whereas the steady state stresses are the same within error (Fig. 2b).

180 The peak shear stress for the coarse-grained sample reached 393 MPa and then weakened to a steady state shear stress of 177 MPa at a shear strain rate of $3.3 \times 10^{-6} s^{-1}$ resulting in a ~55% decrease in stress. The medium-grained
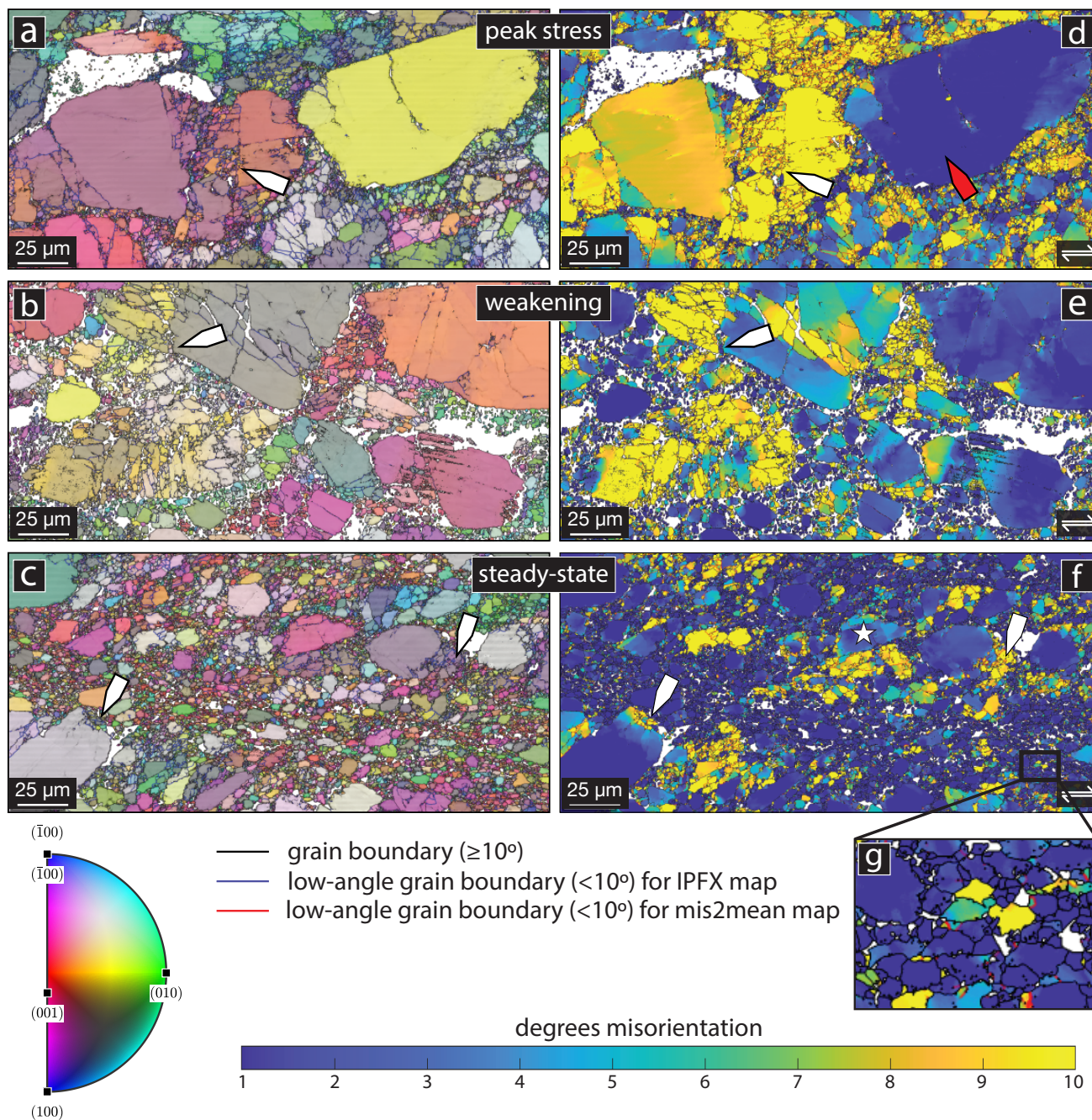
Figure 5. EBSD maps of the strain evolution experiments, with a-c showing inverse pole figures in the x-direction (IPF-X) overlaying band contrast and d-g showing Mis2Mean maps. The white arrows in a) and d) show an example of a pull apart structure. The white arrows in b) and e) show fine grains adjacent to the parent grain and the association of grain size reduction with cleavage planes and fractures. The white arrows in c) and f) show fine grains adjacent to the parent grain that were cataclastically broken off. The red arrow in d) shows relict grains with little to no internal misorientation. g) zoom in of the f) steady state mis2mean map showing bulge microstructures. The white star represents the grain analyzed in Fig. 6
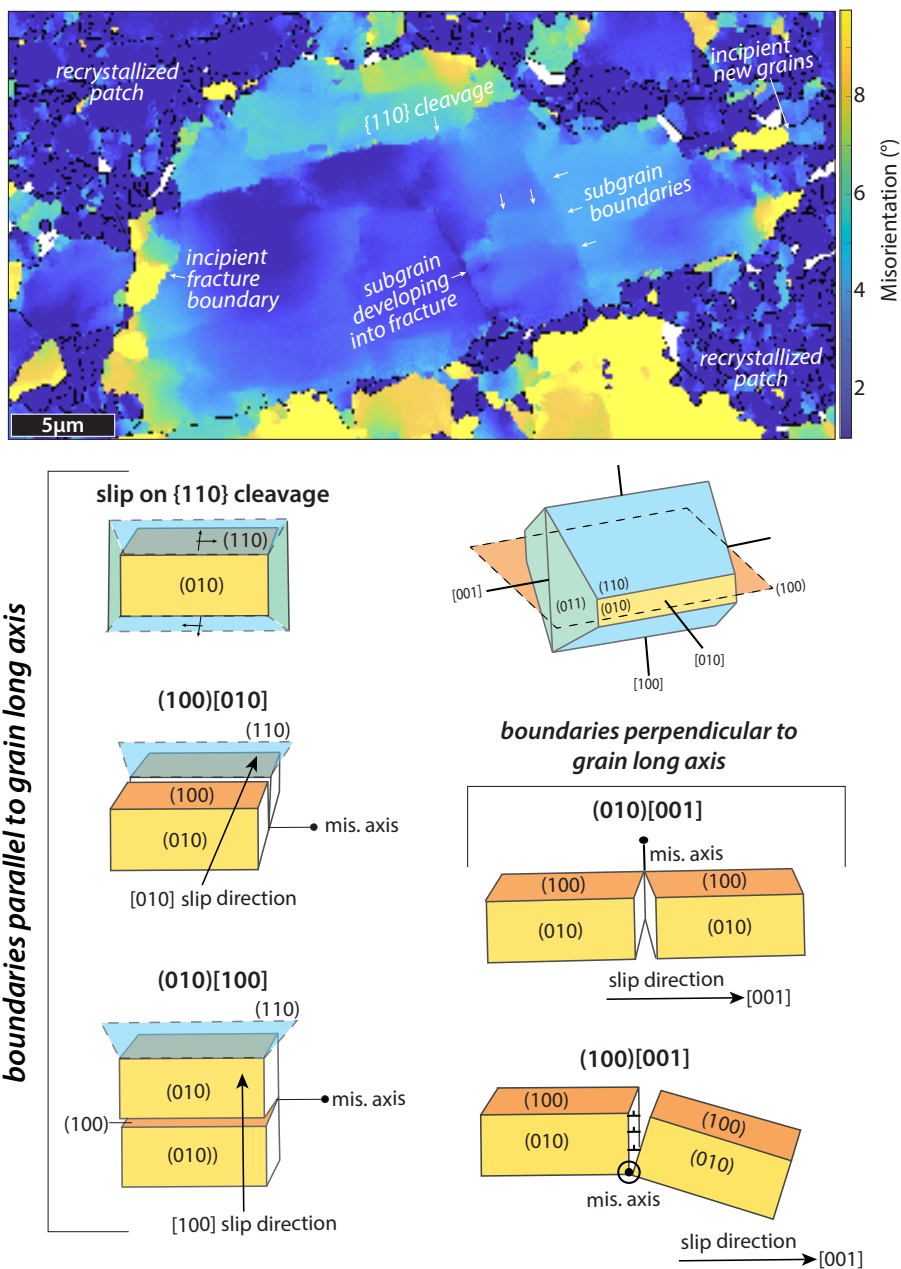
Figure 6. Misorientation (mis2mean) map highlighting an individual relict grain from the medium-grained steady-state sample (see star in Fig. 5f). The grain is surrounded by clusters of newly recrystallized grains and subgrains with high misorientations defining an incipient core-and-mantle structure. The grain interior shows misorientations and subgrains developed both parallel and perpendicular to its long axis. The subgrain boundaries oriented parallel to the grain long axis are compatible with slip on the 110 cleavage, but also with slip on the (100)[010], (010)[100] slip systems. The subgrain boundaries at high angles to the grain long axis are compatible with slip on the (010)[001], and (100)[001] slip systems and do not correspond to amphibole cleavage planes. Amphibole crystal sketch is modified after Jung and Park, 2020.
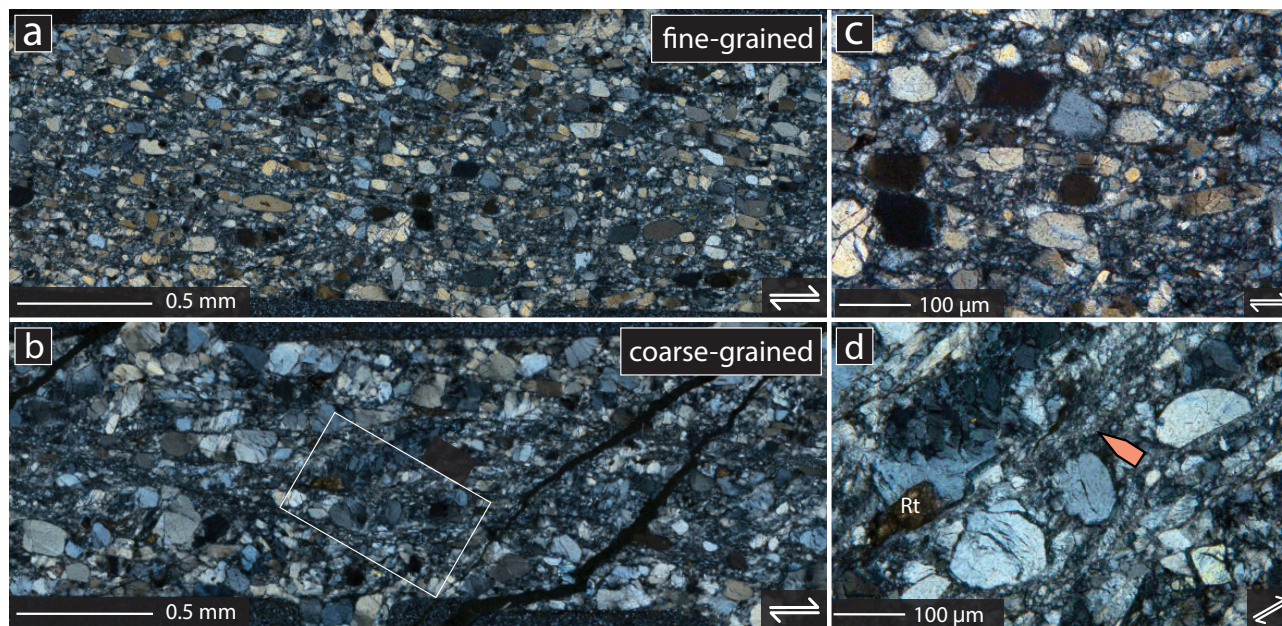
Figure 7. Photomicrographs of the a) fine- and b) coarse-grained fraction samples. c) and d) are zoomed-in photomicrographs from the central regions of the a) fine- and b) coarse-grained samples. White box in b) shows the orientation of d). Orange arrow in d) highlights region of recrystallized matrix. All photomicrographs taken with cross-polarized light and have a dextral shear sense.

sample had a peak shear stress of 283 MPa and reached a steady state shear stress of 158 MPa at a shear strain rate of 3.4×10^{-6}/s resulting in a ~44% decrease in stress. The fine-grained sample had a peak shear stress of 226 MPa and weakened to a steady state shear stress of 171 MPa at a shear strain rate of 3.0×10^{-6}/s resulting in a ~24% decrease in stress. The difference in peak shear stresses for the coarse- and fine-grained size samples is 167 MPa.

3.3.2 Microstructures

The amount of fine-grained material in the matrix is approximately the same regardless of the starting grain size fraction (Fig. 7). However, fine-grained material is more distributed in the fine-grained sample compared to the medium- and course-grained samples (Fig. 7). Relict grains in the fine-grained sample show alignment with the sample-scale foliation with the long axis of the relict grains ranging from parallel to the C'-orientation to parallel to the shear plane, while the relict grains in the medium- and coarse-grained samples show only local or minor foliation development (Fig. 7).

14

3.4 Strain Rate Stepping Experiments

3.4.1 Mechanical Data

195 The strain rate stepping experiments included four to six deformation steps and each step achieved an approximate mechanical steady state (Fig. 2c). The shear stresses and shear strain rates for the $700°C$ experiment range from 145 to 271 MPa and $4.0x10^{-6}$/s to $3.4x10^{-5}$/s, respectively, with a stress exponent of 3.2 ± 0.4 (Fig. 2d). The first and fourth deformation steps were conducted at the same conditions to test reproducibility, producing similar mechanical results (Fig. 2c). The last deformation step was performed at similar deformation conditions to the

200 mechanical data from the constant rate experiments at mechanical steady state, showing strong reproducibility (Fig. 2d). The shear stresses and shear strain rates for the $725°C$ experiment range from 134 to 327 MPa and $1.2x10^{-5}$/s to $6.7x10^{-5}$/s with a stress exponent of 2.0 ± 0.5. The stress exponent for the three lowest stress data points is 2.3 ± 0.7, overlapping with the stress exponent and stress range from the $700°C$ experiment. The shear stresses and shear strain rates for the $750°C$ experiment range from 57 to 189 MPa and $4.7x10^{-6}$/s to $9.6x10^{-5}$/s with a stress

205 exponent of 2.3 ± 0.3; however, the stress exponent for the three highest stress data points is 3.2 ± 0.1, consistent with the $700°C$ sample for a similar stress range (Fig. 2d).

3.4.2 Microstructures

The central portion of the strain rate stepping samples consists of the matrix and a few large relict grains (Fig. 8). These experiments display more recrystallization in the matrix than in the constant rate experiments as they were

210 deformed to higher shear strains. The 700 and $750°C$ samples both show the highest amount of strain is localized to a $\sim$400 μm thick region, defined by the fine-grained matrix (Fig. 8). Some relict grains show recrystallization in intragranular fractures (Fig. 8d, white arrow) while other relict grains show evidence of fracturing, kinking, and bookshelf-slip (Fig. 8b,d, green arrows).

3.5 Interpreted Deformation Mechanisms

215 The mechanical data and microstructural analysis from the suite of experiments described in Section 3 allow us to interpret the deformation processes and mechanisms operating in our samples at both low and high strains. We infer a gradual transition in deformation processes for the three main stages observed in the stress-strain curves (peak stress, weakening, and steady-state). The observations of undulose extinction, kinking, slip on cleavage planes, and grain size reduction to form angular finer-grained aggregates suggest that the peak stress stage is associated

220 with work hardening through both brittle lock-up and dislocation multiplication and glide. The development of incipient fractures and new grains likely occurs in regions of subgrain formation and work hardening in relict grains (Fig. 6). The higher peak stress in the coarser-grained sample is likely due to a) fewer grain orientations available for cleavage slip and/or dislocation glide on accessible slip systems, and b) lower grain boundary area
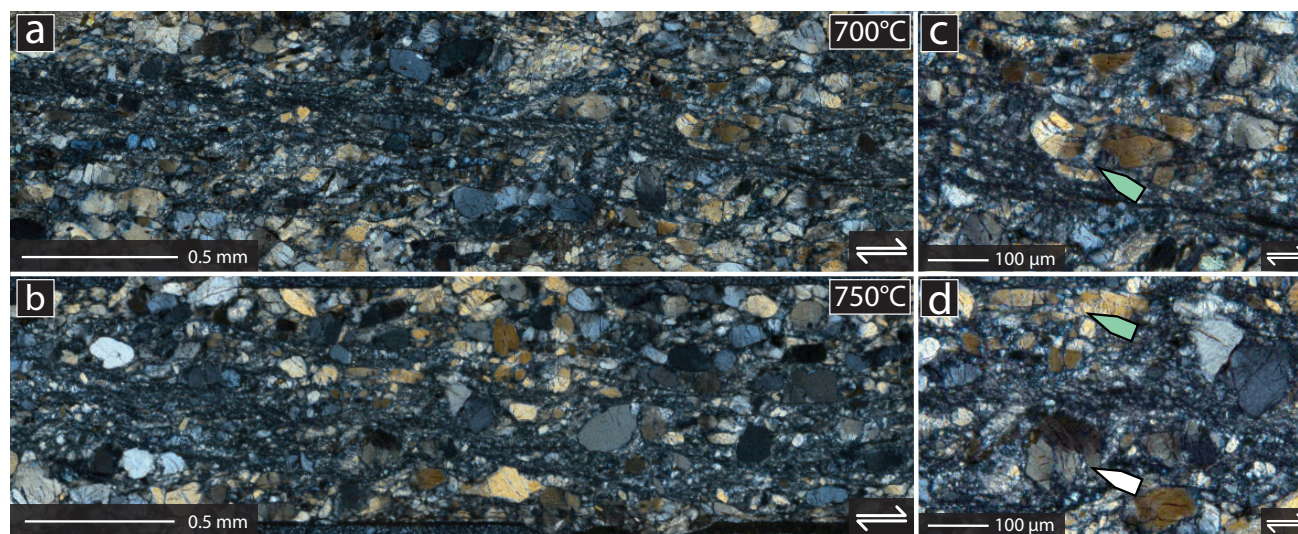
15

Figure 8. Photomicrographs of the strain rate stepping samples conducted at a) $700°C$ and b) $750°C$. c) and d) are zoomed-in photomicrographs from the central portions of the a) $700°C$ and b) $750°C$ samples, respectively. Green arrows in c) and d) highlight kinked relicted grains. White arrow in d) shows an example of recrystallization in a fractured relict grain. All photomicrographs taken with cross-polarized light and have a dextral shear sense.

available to accommodate intergranular rotation and brittle shear. Similar microstructural features observed in the
225 strain-weakened samples suggest that similar processes were operating during that stage, but the greater volume of finer-grained material produced with increasing strain likely allowed more efficient activation of cleavage-slip, granular rotation, and dislocation motion, thus resulting in mechanical weakening. We interpret the mechanical steady state stage to reflect a transition to dislocation creep with limited climb and continued cleavage and fracture slip. This is based on: a) the observation of stress exponents in the strain rate stepping experiments ranging
230 from 2.0 to 3.2 (Fig. 2), b) the absence of a dependence of the steady-state flow stress on the starting grain size, c) increased evidence for dislocation organization in some relict grains in the high strain samples, including subgrain development and incipient core-and-mantle structures (Figs. 5 and 6), d) the presence of localized fine-grained, relatively strain free patches with sutured grain boundaries (Figs. 5 and 7d), and e) changes in the bulk CPO (Fig. 4). We interpret the finer-grained shear zones to be consistent with recovery processes by low-temperature bulge
235 nucleation and grain boundary migration, similar to 'Regime 1' dynamic recrystallization defined for quartz by Hirth and Tullis (1992). In relict grains separation of developing bulges and subgrains into new grains in many cases accommodated by brittle fracture on cleavage, parting, or other fracture planes (e.g. Stipp and Kunze, 2008).

4 DISCUSSION

4.1 Comparison to other Experimental Data

4.1.1 Experiments on other low symmetry minerals

The deformation sequence and processes described in Section 3.5 for our experiments are consistent with other experiments on low-symmetry minerals with prominent cleavage planes. Experiments investigating the brittle-ductile transition in albite and anorthite feldspars, for example, showed prominent strain weakening before achieving mechanical steady state; this sequence was interpreted as initial cataclastic flow followed by dislocation creep (Tullis and Yund, 1987, 1992). Similar to our interpretations, these authors found limited evidence for dislocation climb and interpreted dislocation glide and grain-boundary migration to be the primary deformation and recovery mechanisms activated in feldspar, respectively (Tullis and Yund, 1985, 1987, 1992). In contrast to these observations, experiments on clinopyroxene at brittle-ductile transition conditions show pyroxenes deform primarily by mechanical twinning on the (100) and (001) planes and by 100<001> slip (Kirby and Kronenberg, 1984a; Kronenberg and Shelton, 1980; Kirby and Christie, 1977; AvéLallemant, 1978). An explanation for the difference in mechanical behavior between clinopyroxene and amphibole is that experimental results show mechanical twinning has a lower resolved shear stress than glide at brittle-ductile transition conditions in clinopyroxene (e.g., Figure 6 in AvéLallemant (1978)) than sodic amphibole (Reynard et al., 1989). Experiments near the brittle-ductile transition on higher symmetry, non-tabular, mineral aggregates such as quartz and olivine tend to show less pronounced work hardening/strain weakening, likely due to the lack of prominent cleavage planes, lack of a starting CPO/SPO and an overall greater strain compatibility in the starting material (even for coarse-grained starting materials)(Hirth and Tullis, 1992; Bystricky et al., 2000; Richter et al., 2018; Speciale et al., 2020). Despite differences in the mechanisms and degrees of strain weakening in different minerals, the steady-state processes observed in our experiments involving dislocation glide, grain boundary migration, and fracturing are otherwise common for minerals and metals deformed near their brittle-ductile transition (e.g. Kirby and Kronenberg, 1984b; Tullis and Yund, 1987; Evans et al., 1990; Hirth and Tullis, 1994; Druiventak et al., 2011).

4.1.2 Experiments on Blueschist and Amphibole

Our experiments help define the experimental conditions of the brittle-ductile transition in amphibole, especially when combined with previous experimental studies. Figure 9 compares the equivalent stress, temperature and stress exponent data for experiments that were conducted at the same confining pressure (1.0 GPa) and equivalent strain rate ($\sim 10^{-5} s^{-1}$). At the highest stresses (>1200 MPa), sample-scale faulting is commonly observed with amphibole developing numerous intragranular fractures for temperatures ranging from 300-750$°C$ (Hacker and Christie, 1990; Okazaki and Hirth, 2020). For slightly lower stresses, sample-scale faulting is not observed but brittle to semi-brittle deformation microstructures, such as intragranular fractures and kinking are commonly observed

270 in our peak stress samples (Figs. 5 and 3) as well as in the greenschist and epidote-amphibolite samples by Okazaki and Hirth (2020). Note, the amphibolite samples deformed by Hacker and Christie (1990) also show similar brittle to semi-brittle deformation microstructures but at slightly different deformation conditions than Figure 9a. The transition from brittle to ductile deformation in these samples at steady state conditions generally occurs at stresses of ~550-600 MPa with samples showing dislocation and diffusion creep microstructures at equivalent stresses
275 between 100-500 MPa and equivalent strain rates of ~1.0×10^{-5}/s (Fig. 9a). This change in deformation mechanisms at these conditions is also confirmed by the change in stress exponent, from greater than 20 in Okazaki and Hirth (2020) to ~3 from our data and Hacker and Christie (1990) to less than 3 in Tokle et al. (2023a) and Getsinger and Hirth (2014) (Fig. 9b). To further illustrate the change in deformation mechanisms in sodic amphiboles, at $700°C$ in Figure 9a there is a change from brittle microstructures at stresses of ~1000 MPa to dislocation creep
280 microstructures at stresses of ~500 MPa and then diffusion creep microstructures at stresses of ~250 MPa and lower. In addition to being mechanically weaker, the diffusion creep samples also have a lower stress exponent relative to the dislocation creep samples (Fig. 10b). We note that the diffusion creep experiments from Tokle et al. (2023a) are a polyphase blueschist aggregate, whereas our samples are a pure glaucophane aggregate which may affect where the transition between diffusion and dislocation creep occurs; however, in both samples amphibole
285 was the rheologically controlling mineral.

The specific grain-scale deformation processes that we observe in our experiments during both the work hardening/strain weakening stages and the steady state creep phase have also been observed in other experimental studies on sodic amphiboles. General shear deformation experiments on a natural epidote blueschist show microstructural evidence in grains larger than 30 μm that grain size reduction via brittle fracturing as well as local
290 misorientation is interpreted to derive from dislocation activity, which is consistent with processes we observe in our relict grains (see Fig. 6 in Park et al. (2020)) (Figs. 5 and 6). General shear deformation experiments on a lawsonite blueschist show the development of subgrains and stacking faults in fine-grained glaucophane, suggesting dislocation glide as well as climb are active, which is again consistent with our observations (Kim et al., 2015).

4.1.3 CPO Development in Experimental Samples

295 Several experimental studies have focused on linking CPO development and seismic anisotropy in amphibole-bearing rocks to deformation conditions relevant to the subduction interface (Ko and Jung, 2015; Kim et al., 2013; Ha et al., 2019; Kim and Jung, 2019; Park and Jung, 2022). Amphibole CPOs have been classified into four primary types based on CPO geometry from general shear deformation experiments (Ko and Jung, 2015; Kim and Jung, 2019) (Fig.4). Types 1-3 have been produced in experiments to shear strains <3 and are interpreted to correspond
300 to different temperatures and differential stresses (Ko and Jung, 2015). The Type 4 CPO has only been documented in deformation experiments in fine-grained samples deformed to shear strains >3 (Kim and Jung, 2019). The CPOs documented in these experiments were not well linked to deformation process[es], e.g. rigid body rotation, cataclastic flow, dislocation glide, and dislocation or diffusion creep, because mechanical and detailed microstructural
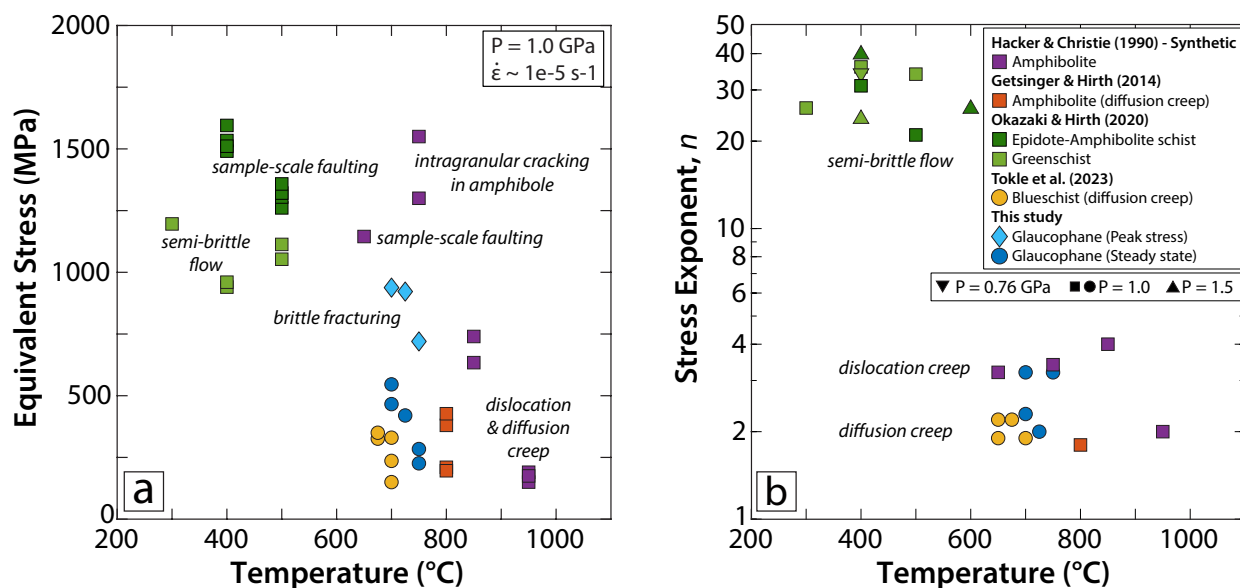
Figure 9. Plots of temperature versus stress and temperature versus stress exponent for mafic schists, blueschists, and glauco-phane. a) Comparison highlighting the high stresses accessed during peak stress conditions associated with brittle deformation and the lower flow stresses during dislocation creep. b) Comparison showing semi-brittle deformation associated with stress exponents >20 and diffusion mechanisms associated with lower stress exponents. (Hacker and Christie, 1990; Getsinger and Hirth, 2014; Okazaki and Hirth, 2020; Tokle et al., 2023a)

data were not presented in those studies. Additionally, the differences among Types 1, 2, and 3 are subtle——i.e.
305   distinguishing among diffuse girdles or diffuse point maxima of the [010] and [001] axes can be arbitrary and likely
depends on EBSD map quality and size, cleaning and grain selection routines, and whether or not pole figures
are presented point-per-grain. It is also unclear how the Type 4 CPO defined by Kim and Jung (2019) can have a
(010) and (001) maximum while the (110) and (100) have girdles as this pole figure configuration is not crystal-
lographically consistent. Figure 4 shows a modified Type 4 CPO with a (010) girdle. Conservatively, our samples
310   show mixtures of Type 1 and 3, with the (110) and (100) showing point maxima perpendicular to the shear plane
and (010) and (001) showing diffuse point maxima or girdles lying in the shear plane (Fig. 4). The conditions of
our experiments would predict a Type 2 CPO based on the classification of Ko and Jung (2015), which is inconsis-
tent with what we observe (Fig. 4). The mixed Type 1/3 CPOs present in the hydrostatic and peak stress samples
indicate that this fabric can be produced by rigid rotation and cataclasis. We also note that a Type 1/3 fabric was
315   observed by Tokle et al. (2023a) for diffusion creep in experimentally deformed blueschist samples. The transition
to a more definitive Type 1 CPO in our mechanical steady-state samples that reached $\gamma \sim 2$ suggests that this CPO is
also consistent with dislocation creep. This is because the activation of slip systems compatible with our subgrain
orientations, such as (100)[001] slip (Fig. 6), would not be expected to lead to a major reorientation of the CPO from

320 the original hydrostatic CPO developed by rotation (Fig. 4). Thus our data support the general notion that CPO in tabular minerals is not a diagnostic indicator of deformation mechanisms such as dislocation or diffusion creep.

4.2   Comparison to Observations from Natural Rocks

The microstructures and interpreted deformation mechanisms in our experiments also bear close similarities to naturally deformed amphibole-bearing rocks. The observed work hardening and subsequent grain size reduction and cataclasis accommodated by kinking, cleavage-slip, and micro-domino rotation during peak and weakening
325 stresses in our experiments is consistent with several studies documenting these processes at relatively high stresses (or fast strain rates) in amphibole (Allison and La Tour, 1977; Babaie and La Tour, 1994; Brückner and Trepmann, 2021). Nyman et al. (1992), for example, described hornblende-bearing amphibolites deformed at ∼500°C that appear to show initial dislocation glide in amphibole, followed by dislocation buildups at cleavages and grain boundaries and eventual grain size reduction by cataclasis. Kinking of amphibole to orient grains into more favorable slip
330 orientations was shown in Brückner and Trepmann (2021). The development of microdomino textures are documented in naturally deformed amphiboles (Allison and La Tour, 1977; Babaie and La Tour, 1994) where fracturing occurs subnormal to the c axis localizing strain on specific slip planes, such as the {110} cleavage plane (Allison and La Tour, 1977). Examples of blueschist specifically from subduction settings deformed via cataclastic mechanisms are also documented for several localities, including the northern Cascades (USA) (Misch, 1969), the Zagros Moun-
335 tains (Iran) (Muñoz-Montecinos et al., 2021; Muñoz-Montecinos et al., 2023), and the Ryukyu arc (Japan) (Imon et al., 2004). Some studies furthermore describe brittle deformation in amphibole as a precursor to longer-term viscous deformation (Muñoz-Montecinos et al., 2023).

Evidence for dislocation activity/creep in sodic amphibole is also documented for several natural settings. Reynard et al. (1989), for example, examined slip systems in sodic amphibole from rocks in the western Alps deformed
340 at relatively low (350-450°C) and high (550-600°C) temperatures. For the high temperature samples, these authors interpreted dislocation climb-controlled creep based on TEM analyses revealing the operation of glide on multiple slip systems and the organization of dislocations into discrete subgrain walls. For the lower temperature samples, only the (010)[001] slip system appeared to be activated in glaucophane— this is one of the same slip systems inferred for weakly developed subgrain boundaries in our experimental samples (Fig. 6). The dynamically re-
345 crystallized grains are described as fine-grained (<50 μm) and irregular in shape compared to larger undeformed grains exhibiting undulose extinction, which is comparable to the bimodal grain sizes we find in our samples (Fig. 5) (Reynard et al., 1989). Similar evidence for dislocation activity is documented for glaucophane approaching eclogite-facies conditions on Syros Island (Greece) (Behr et al., 2018; Kotowski and Behr, 2019), the Diablo Range (USA) (Kim et al., 2013), and Corsica Island (France) (Choi et al., 2024). The CPOs observed in samples from these
350 localities is consistent with Type 1, as observed in our mechanical steady-state experiments (Fig. 4). This CPO is the most commonly observed CPO in naturally deformed amphibole-bearing rocks and appears consistent with both

rigid rotation and dislocation creep mechanisms (Shaocheng et al., 1993; Berger and Stünitz, 1996; Díaz Aspiroz et al., 2007; Tatham et al., 2008; Getsinger et al., 2013; Ji et al., 2013; Ott et al., 2024).

4.3 A Flow Law for Dislocation Creep in Glaucophane

355 Our strain rate stepping experiments conducted at different temperatures allow us to construct a dislocation creep flow law for glaucophane. While the stress exponents from the strain rate stepping experiments range from 2.0-3.2, we assume a value of $n = 3$, consistent with the theoretical value for dislocation creep (i.e., Poirier (1985)) and within the uncertainty of our mechanical data (Fig. 2). The remaining parameters are fit using a least squares regression to the equation:

360
$$\dot{\varepsilon} = A\sigma^n exp\left(\frac{-Q}{RT}\right)$$

where $\dot{\varepsilon}$ is strain rate in s^{-1}, A is the material parameters in $MPa^{-n}s^{-1}$, σ is the differential stress in MPa, n is the stress exponent, Q is the activation energy in kJ/mol, R is the gas constant, and T is temperature in K. This provides flow law parameters of $Q = 341\pm 37$ kJ/mol and $A = 2.23$x10^5 MPa^{-n} s^{-1}, where uncertainty in Q is reported as one standard deviation. Plotting the flow law against the strain rate stepping data shows good

365 agreement with both the strain rate stepping experiments as well as the constant rate experiments (Fig. 10a). The lowest stress data point from the $750°C$ experiment is weaker than predicted by the flow law and may indicate a transition to a lower-stress mechanism such as diffusion creep (Fig. 10a), while the highest stress data point in the $725°C$ experiment may represent peak stress conditions, given that many deformation steps at similar stress magnitudes where the strain rate was increased show a peak stress followed by strain weakening to a steady

370 state value, indicating this data point may be an overestimate of the steady state stress (Fig. 2). For comparison, we plot the $700°C$ strain rate stepping mechanical data for the dislocation creep samples from this study and the diffusion creep via microboudinage in blueschist mechanical data from Tokle et al. (2023a) (Fig. 10b). Here we show that for a given strain rate, the diffusion creep mechanism deforms at lower stresses than the dislocation creep mechanism, consistent with general theory that diffusional mechanisms operate at lower stresses relative

375 to dislocation mechanisms (Frost and Ashby, 1982). Additionally, we highlight the magnitude of the activation enthalpy term (341 ± 37 kJ/mol) is within the uncertainty of the activation enthalpy for blueschist diffusion creep experiments (384 ± 15 kJ/mol; (Tokle et al., 2023a)).

4.4 Application to Subducting Slab and Subduction Interface Rheology

The prominent strain weakening that we observe in our experiments has several important implications for sub-
380 ducting oceanic crust deforming to relatively low strains at blueschist facies conditions. Firstly, the dependency of both the peak strength and the magnitude of strain weakening on grain size implies that oceanic crustal pro-
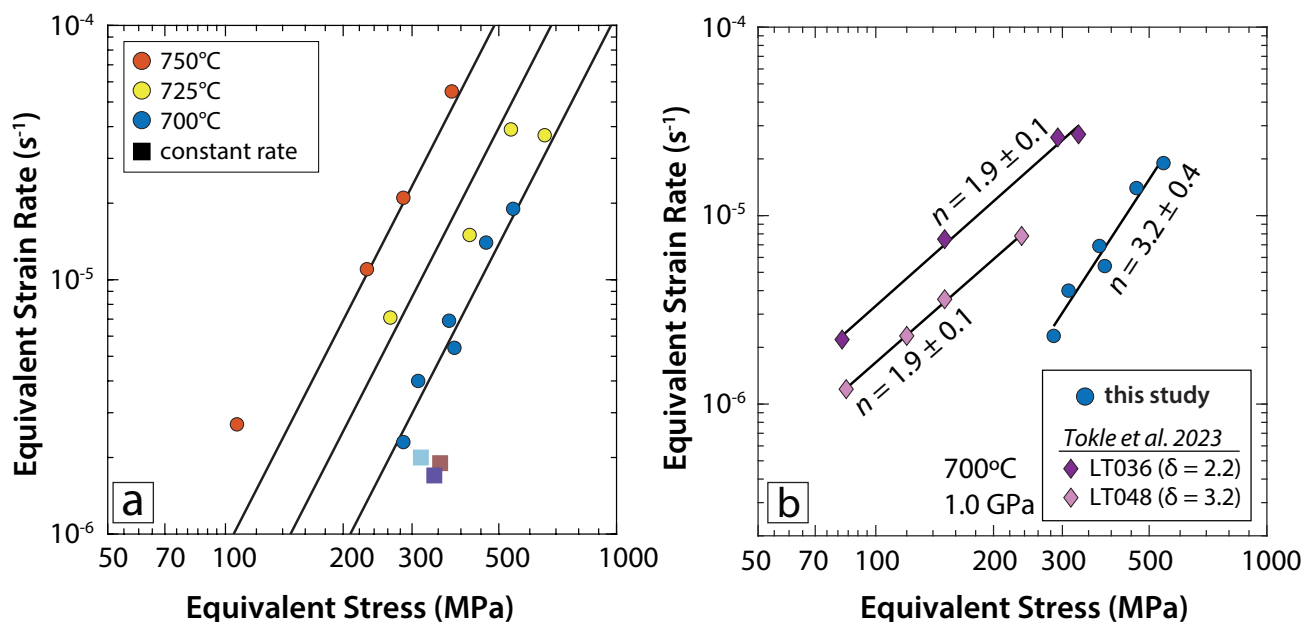
Figure 10. a) Fitting the 700, 725, and $750°C$ strain rate stepping experiments to a n = 3 power law. The three constant rate experiments that achieved a mechanical steady state are also plotted to show consistency between the strain rate stepping and constant rate experiments. b) Comparison between blueschist deformation experiments deforming by diffusion creep (Tokle et al., 2023a) and glaucophane deformed for this study.

toliths of similar compositions but different grain sizes will exhibit different mechanical behaviors at low strains. Coarse-grained intrusive igneous protoliths such as gabbros, for example, will require greater stress concentrations for brittle yielding, and upon yielding, these rocks will exhibit more pronounced strain weakening compared to

385 finer-grained basaltic dikes/flows or zones of substantial seafloor alteration. Secondly, the observation that brittle deformation and strain weakening is a precursory step to initiate dislocation creep implies that if the brittle yield strength in certain subducted rocks is not achieved, dislocation creep mechanisms will also likely remain inaccessible. This may explain the common preservation of nearly undeformed coarse-grained blueschists with relict igneous intrusive textures to blueschist facies and beyond in subduction settings (e.g., Rubie (1983); Philippot and

390 van Roermund (1992); Hacker (1996); Clarke et al. (1997); Angiboust et al. (2011); Hunziker et al. (2017); Kotowski and Behr (2019)). Thirdly, our experiments indicate that a shear strain of approximately 0.75 is sufficient to initiate strain weakening and a transition to dislocation creep in oceanic crust. This amount of strain is relatively low and if the brittle yield strength is exceeded, this strain can be accumulated through common brittle deformation events, such as megathrust earthquakes, intra-slab earthquakes at the slab's upper boundary, or low-frequency

395 earthquakes in the tremor-producing zone. Given the characteristic displacements associated with these events, ranging from centimeters for LFEs to meters for larger earthquakes (Schmidt and Gao, 2010; Nishimura et al., 2013; Michel et al., 2019; Radiguet et al., 2012; Ozawa, 2017; Takagi et al., 2019; Rousset et al., 2019; Bostock et al., 2015;

Thomas et al., 2016; Chestler and Creager, 2017), the required strain could be accumulated within just a few typical earthquake or slow slip and tremor cycles for km-scale oceanic blocks or lenses. Although exact lengthscales

400 are unknown, this implies that brittle deformation in coarse-grained oceanic crust at blueschist facies conditions can persist over multiple earthquake cycles but is otherwise expected to be short/transient on long-term geologic timescales.

To consider the implications of our experiments for longer-term (larger strain) deformation of mafic oceanic crust under blueschist facies conditions, we can examine the extrapolation of steady-state blueschist flow laws to nat-

405 ural conditions. The flow laws presented in Section 4.3 and in Tokle et al. (2023a) are the two that have thus far been developed for blueschists, with our flow law constraining dislocation creep and the Tokle et al. (2023a) flow law representing diffusion creep where the diffusion lengthscale is controlled by the spacing of boudins/fractures in amphibole. Figure 11 shows deformation mechanism maps for these two flow laws in stress-temperature and stress-boudin spacing space. Similar to other minerals such as quartz and olivine (Frost and Ashby, 1982; Warren

410 and Hirth, 2006; Austin and Evans, 2007), the maps show that diffusion creep is favored at lower stresses, higher temperatures, and finer boudin spacings (i.e., diffusion length scale) than the dislocation creep mechanism. For temperatures below $\sim$450$^\circ C$ and stresses less than 1 GPa, strain rates for both mechanisms are much lower than would be expected for subduction plate boundaries (e.g. 1x10^{-12}/s to 1x10^{-14}/s). Given that deviatoric stress magnitudes in subduction zones are typically estimated to be under 100 MPa (Lamb, 2006; Behr and Platt, 2013; Penney

415 et al., 2017; Sibson, 2017; Li et al., 2018; Schmidt and Platt, 2022), it seems likely that brittle-plastic deformation or other mechanisms not captured by these two flow laws would dominate in low-temperature mafic blueschists. Overall these deformation mechanism maps provide a quantitative framework for investigating deformation in natural blueschists and predicting which mechanism is expected to dominate under which conditions as a function of rock properties, strain rate, and subduction thermal gradients.

420 Our flow law also has implications for the long term strength/viscosity of blueschist-facies oceanic crust relative to other potential subduction input materials and metamorphic conditions. Figure 12 shows viscosity versus temperature for a constant strain rate of 1×10^{-12} s^{-1} and a range of flow laws that represent e.g. sediments (quartz dislocation creep (Tokle et al., 2019)), blueschist-facies metamafic rocks (this study and the Tokle et al. (2023a) flow law), and eclogite-facies metamafic rocks (eclogite dislocation creep (Zhang and Green, 2007)). The two blueschist

425 flow laws show intermediate viscosities between those for quartz and eclogite– this is consistent with the rheological hierarchy that would be inferred qualitatively from observations of block-and-matrix structures in subduction melanges (Davis and Whitney, 2006; Cao et al., 2013; Kotowski and Behr, 2019). For the strain rate shown in (Fig. 12), the viscosity for blueschists does not approach that of quartz until $\sim$600$^\circ C$, which is also the temperature expected for the complete breakdown of blueschist to form eclogite (Evans, 1990). Thus, blueschists are expected to remain

430 strong relative to quartz-rich rocks over their entire stability field. The viscosity contrast between blueschist creep mechanisms and quartz dislocation creep is 1-2 orders of magnitude on average over the blueschist temperature range. A viscosity range of $\sim$10^{-18} to 10^{-20} Pa·s is consistent with the range expected to still permit steady-state
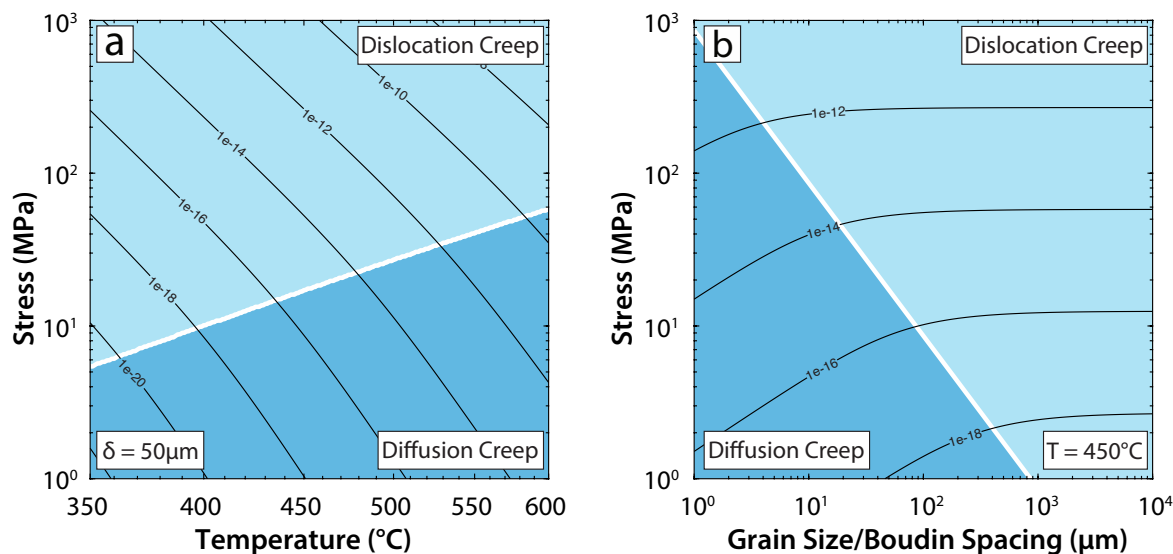
Figure 11. Deformation mechanism maps comparing the dislocation creep (this study) and diffusion creep limited by microboudinage flow laws (Tokle et al., 2023a) with strain rates represented by the contour lines. a) Temperature versus stress at a boudin spacing of 50 μm for the diffusion creep flow law. b) Grain size/boudin spacing (for the diffusion creep law) versus stress. The deformation mechanism map codes used to generate the figures are modified from (Warren and Hirth, 2006)

subduction, but lower viscosities should promote faster subduction velocities and vice versa (Behr et al., 2022; Behr and Becker, 2018). Thus, the viscosities predicted by our flow law support the suggestion that sediment- or

435 serpentinite-rich subduction interfaces should be weaker than those dominated by mafic oceanic crust (sediment-starved) and should promote faster slab sinking, overriding plate rollback and convergence velocities (Behr et al., 2022).

5 Conclusions

Constant rate and strain-rate-stepping experiments on glaucophane aggregates of varying grain sizes show that de-

440 formation in glaucophane occurred in three stages: 1) an early stage of work hardening associated with brittle lock-up and dislocation accumulation, 2) a second stage of prominent strain weakening associated with brittle fracture and cataclasis, slip on cleavage planes, and dislocation glide, and 3) a transition to dislocation creep with limited climb at mechanical steady-state, defined by dynamic recrystallization by bulge nucleation and fracture-enhanced subgrain rotation. The peak stress and magnitude of strain weakening in the experiments was a function of starting

445 grain size whereas the steady-state stress was independent of grain size. The switch from brittle-dominated deformation to a dislocation-related deformation mechanism is consistent with experimentally and naturally deformed samples of other low-symmetry minerals. The strain rate stepping experiments had stress exponents ranging from
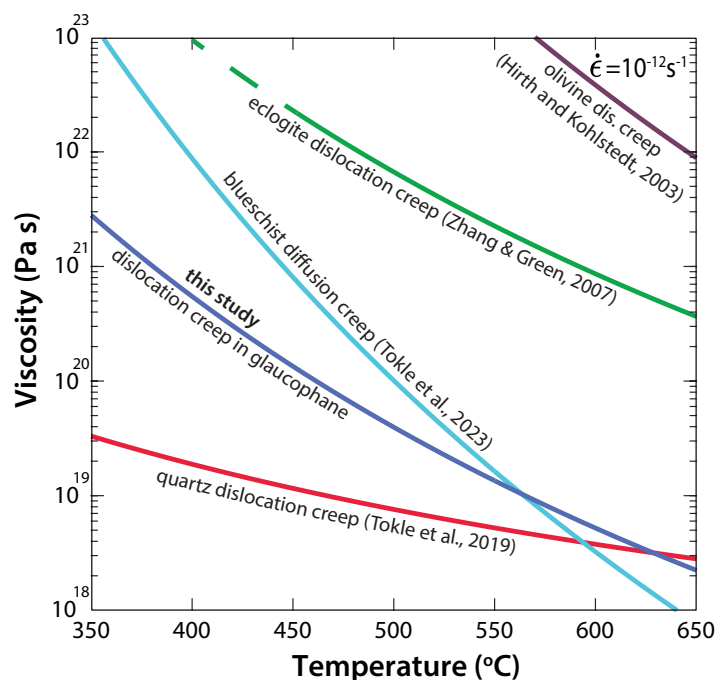
Figure 12. Viscosity versus temperature plot at a constant strain rate of $1\mathrm{x}10^{-12}$/s comparing the strength of the glaucophane dislocation creep flow law with other strain-accommodating materials associated with glaucophane: quartz (Tokle et al., 2019) , blueschist aggregates (Tokle et al., 2023a), and eclogite (Zhang and Green, 2007). Olivine is included for comparison (Hirth and Kohlstedt, 2003).

2.0-3.2 which we used to produce a dislocation creep flow law with a Q of 341 ± 37 kJ/mol and an A of 2.23×10^5 $\mathrm{MPa}^{-n}\mathrm{s}^{-1}$ for a n of 3. Comparison of this flow law to a diffusion creep flow law for sodic amphibole (Tokle et al.,

450 2023a) indicates dislocation creep should dominate at higher stresses, lower temperatures and larger diffusion lengthscales. The flow law implies that for conditions where blueschists are stable, the viscosity of sodic amphibole is stronger than quartz and weaker than eclogite.

Data availability.

The data from this work is available at https://doi.org/10.3929/ethz-b-000671272.

455 *Author contributions.*

Conceptualization: Whitney M. Behr, Leif Tokle, Lonnie J. Hufford Data Curation: Lonnie J. Hufford, Leif Tokle, Luiz F. G. Morales Formal Analysis: Lonnie J. Hufford, Leif Tokle, Whitney Behr Software: Claudio Madonna Su-

pervision: Leif Tokle, Whitney M. Behr Visualization: Lonnie J. Hufford, Leif Tokle, Whitney M. Behr Writing-
original draft: Lonnie J. Hufford, Leif Tokle, Whitney M. Behr Writing- review and editing: Lonnie J. Hufford, Leif

460 Tokle, Whitney M. Behr, Luiz F. G. Morales, Claudio Madonna

Competing interests.

The authors declare that they have no competing interests.

465 **References**

Allison, I. and La Tour, T. E. (1977). Brittle deformation of hornblende in a mylonite: a direct geometrical analogue of ductile deformation by translation gliding. *Canadian Journal of Earth Sciences*, 14(8):1953–1958.

Angiboust, S., Agard, P., Raimbourg, H., Yamato, P., and Huet, B. (2011). Subduction interface processes recorded by eclogite-facies shear zones (Monviso, W. Alps). *Lithos*, 127(1-2):222–238.

470 Austin, N. J. and Evans, B. (2007). Paleowattmeters: A scaling relation for dynamically recrystallized grain size. *Geology*, 35(4):343–346.

AvéLallemant, H. G. (1978). Experimental deformation of diopside and websterite. *Tectonophysics*, 48(1-2):1–27.

Babaie, H. A. and La Tour, T. E. (1994). Semibrittle and cataclastic deformation of hornblende-quartz rocks in a ductile shear zone. *Tectonophysics*, 229(1-2):19–30.

475 Behr, W. M. and Becker, T. W. (2018). Sediment control on subduction plate speeds. *Earth and Planetary Science Letters*, 502:166–173.

Behr, W. M., Holt, A. F., Becker, T. W., and Faccenna, C. (2022). The effects of plate interface rheology on subduction kinematics and dynamics. *Geophysical Journal International*, 230(2):796–812.

Behr, W. M., Kotowski, A. J., and Ashley, K. T. (2018). Dehydration-induced rheological heterogeneity and the deep tremor 480 source in warm subduction zones. *Geology*, 46(5):475–478.

Behr, W. M. and Platt, J. P. (2013). Rheological evolution of a mediterranean subduction complex. *Journal of Structural Geology*, 54:136–155.

Berger, A. and Stünitz, H. (1996). Deformation mechanisms and reaction of hornblende: Examples from the Bergell tonalite (Central Alps). *Tectonophysics*, 257(2-4 SPEC. ISS.):149–174.

485 Bostock, M. G., Thomas, A. M., Savard, G., Chuang, L., and Rubin, A. M. (2015). Magnitudes and moment-duration scaling of low-frequency earthquakes beneath southern Vancouver Island. *Journal of Geophysical Research: Solid Earth*, 120(9):6329–6350.

Braden, Z. and Behr, W. M. (2021). Weakening mechanisms in a basalt-hosted subduction megathrust fault segment, southern alaska. *Journal of Geophysical Research: Solid Earth*, 126(9):e2021JB022039.

Brückner, L. M. and Trepmann, C. A. (2021). Stresses during pseudotachylyte formation-evidence from deformed amphibole 490 and quartz in fault rocks from the silvretta basal thrust (austria). *Tectonophysics*, 817:229046.

Bystricky, M., Kunze, K., Burlini, L., and Burg, J.-P. (2000). High shear strain of olivine aggregates: Rheological and seismic consequences. *Science*, 290(5496):1564–1567.

Cao, Y., Jung, H., and Song, S. (2013). Petro-fabrics and seismic properties of blueschist and eclogite in the north qilian suture zone, nw china: Implications for the low-velocity upper layer in subducting slab, trench-parallel seismic anisotropy, and 495 eclogite detectability in the subduction zone. *Journal of Geophysical Research: Solid Earth*, 118(6):3037–3058.

Chauve, T., Montagnat, M., Barou, F., Hidas, K., Tommasi, A., and Mainprice, D. (2017). Investigation of nucleation processes during dynamic recrystallization of ice using cryo-EBSD. *Philosophical Transactions of the Royal Society A: Mathematical, Physical and Engineering Sciences*, 375(2086).

Chestler, S. R. and Creager, K. C. (2017). Evidence for a scale-limited low-frequency earthquake source process. *Journal of* 500 *Geophysical Research: Solid Earth*, 122(4):3099–3114.

Choi, S. et al. (2024). Deformation microstructures of blueschists in alpine corsica, france, and implications for seismic anisotropy and the low-velocity layer in subducting oceanic crust. *Tectonophysics*, Preproof:Preproof.

Clarke, G. L., Aitchison, J. C., and Cluzel, D. (1997). Eclogites and blueschists of the Pam Peninsula, NE New Caledonia: A reappraisal. *Journal of Petrology*, 38(7):843–876.

Cowan, D. S. (1978). Origin of blueschist-bearing chaotic rocks in the franciscan complex, san simeon, california. *GSA Bulletin*, 89(9):1415–1423.

Davis, P. B. and Whitney, D. (2006). Petrogenesis of lawsonite and epidote eclogite and blueschist, sivrihisar massif, turkey. *Journal of Metamorphic Geology*, 24(9):823–849.

De Caroli, S. et al. (2024). Deformation microstructures of low- and high-strain epidote-blueschist (ryukyu arc, japan): Implications for subduction interface rheology. *Journal of Structural Geology*, 180:105041.

Díaz Aspiroz, M., Lloyd, G. E., and Fernández, C. (2007). Development of lattice preferred orientation in clinoamphiboles deformed under low-pressure metamorphic conditions. A SEM/EBSD study of metabasites from the Aracena metamorphic belt (SW Spain). *Journal of Structural Geology*, 29(4):629–645.

Druiventak, A., Trepmann, C. A., Renner, J., and Hanke, K. (2011). Low-temperature plasticity of olivine during high stress deformation of peridotite at lithospheric conditions—an experimental study. *Earth and Planetary Science Letters*, 311(3-4):199–211.

Ernst, W. (2016). Franciscan mélanges: Coherent blocks in a low-density, ductile matrix. *International Geology Review*, 58(5):626–642.

Evans, B., Fredrich, J. T., and Wong, T.-F. (1990). The brittle-ductile transition in rocks: Recent experimental and theoretical progress. *The brittle-ductile transition in rocks*, 56:1–20.

Evans, B. W. (1990). Phase relations of epidote-blueschists. *Lithos*, 25(1-3):3–23.

Frost, H. J. and Ashby, M. F. (1982). *Deformation-mechanism maps: the plasticity and creep of metals and ceramics*.

Getsinger, A. and Hirth, G. (2014). Amphibole fabric formation during diffusion creep and the rheology of shear zones. *Geology*, 42(6):535–538.

Getsinger, A. J., Hirth, G., Stünitz, H., and Goergen, E. T. (2013). Influence of water on rheology and strain localization in the lower continental crust. *Geochemistry, Geophysics, Geosystems*, 14(7):2247–2264.

Ha, Y., Jung, H., and Raymond, L. A. (2019). Deformation fabrics of glaucophane schists and implications for seismic anisotropy: the importance of lattice preferred orientation of phengite. *International Geology Review*, 61(6):720–737.

Hacker, B. R. (1996). Eclogite formation and the rheology, buoyancy, seismicity, and H2O content of oceanic crust. *Geophysical Monograph Series*, 96:337–346.

Hacker, B. R. and Christie, J. M. (1990). Brittle/ductile and plastic/cataclastic transitions in experimentally deformed and metamorphosed amphibolite. *The Brittle-Ductile Transition in Rocks*, 56:127–147.

Hefferan, K. P., Admou, H., Hilal, R., Karson, J. A., Saquaque, A., Juteau, T., Bohn, M. M., Samson, S. D., and Kornprobst, J. M. (2002). Proterozoic blueschist-bearing mélange in the anti-atlas mountains, morocco. *Precambrian Research*, 118(3-4):179–194.

Hirth, G. and Kohlstedt, D. L. (2003). Rheology of the Upper Mantle and the Mantle Wedge: a View From the Experimentalists BT - Geophysical Monograph Series. *Geophysical Monograph Series*, 138:83–106.

Hirth, G. and Tullis, J. (1992). Dislocation creep regimes in quartz aggregates. *Journal of structural geology*, 14(2):145–159.

Hirth, G. and Tullis, J. (1994). The brittle-plastic transition in experimentally deformed quartz aggregates. *Journal of Geophysical Research: Solid Earth*, 99(B6):11731–11747.

540 Holyoke III, C. W. and Kronenberg, A. K. (2010). Accurate differential stress measurement using the molten salt cell and solid salt assemblies in the griggs apparatus with applications to strength, piezometers and rheology. *Tectonophysics*, 494(1-2):17–31.

Hunziker, D., Burg, J. P., Moulas, E., Reusser, E., and Omrani, J. (2017). Formation and preservation of fresh lawsonite: Geothermobarometry of the North Makran Blueschists, southeast Iran. *Journal of Metamorphic Geology*, 35(8):871–895.

Ildefonse, B., Lardeaux, J.-M., and Caron, J.-M. (1990). The behavior of shape preferred orientations in metamorphic rocks:
545 amphiboles and jadeites from the monte mucrone area (sesia-lanzo zone, italian western alps). *Journal of Structural Geology*, 12(8):1005–1011.

Imon, R., Okudaira, T., and Kanagawa, K. (2004). Development of shape-and lattice-preferred orientations of amphibole grains during initial cataclastic deformation and subsequent deformation by dissolution–precipitation creep in amphibolites from the ryoke metamorphic belt, sw japan. *Journal of Structural Geology*, 26(5):793–805.

550 Incel, S. et al. (2017). Laboratory earthquakes triggered during eclogitization of lawsonite-bearing blueschist. *Earth and Planetary Science Letters*, 459:320–331.

Jenkins, D. et al. (2010). Compressibility of synthetic glaucophane. *Phys Chem Minerals*, 37:219–226.

Ji, S., Shao, T., Michibayashi, K., Long, C., Wang, Q., Kondo, Y., Zhao, W., Wang, H., and Salisbury, M. H. (2013). A new calibration of seismic velocities, anisotropy, fabrics, and elastic moduli of amphibole-rich rocks. *Journal of Geophysical Research:*
555 *Planets*, 118(9):4699–4728.

Kim, D. et al. (2013). Rheological contrast between glaucophane and lawsonite in naturally deformed blueschist from d iablo r ange, c alifornia. *Island Arc*, 22(1):63–73.

Kim, D. et al. (2015). Deformation microstructures of glaucophane and lawsonite in experimentally deformed blueschists: Implications for intermediate-depth intraplate earthquakes. *J. Geophys. Res. Solid Earth*, 120:1229–1242.

560 Kim, J. and Jung, H. (2019). New crystal preferred orientation of amphibole experimentally found in simple shear. *Geophysical Research Letters*, 46(22):12996–13005.

Kirby, S. H. and Christie, J. M. (1977). Mechanical twinning in diopside Ca(Mg,Fe)Si2O6: Structural mechanism and associated crystal defects. *Physics and Chemistry of Minerals*, 1(2):137–163.

Kirby, S. H. and Kronenberg, A. K. (1984a). Deformation of clinopyroxenite: evidence for a transition in flow mechanisms and
565 semibrittle behavior. *Journal of Geophysical Research*, 89(B5):3177–3192.

Kirby, S. H. and Kronenberg, A. K. (1984b). Deformation of clinopyroxenite: Evidence for a transition in flow mechanisms and semibrittle behavior. *Journal of Geophysical Research: Solid Earth*, 89(B5):3177–3192.

Ko, B. and Jung, H. (2015). Crystal preferred orientation of an amphibole experimentally deformed by simple shear. *Nature communications*, 6(1):6586.

570 Kotowski, A. J. and Behr, W. M. (2019). Length scales and types of heterogeneities along the deep subduction interface: Insights from exhumed rocks on syros island, greece. *Geosphere*, 15(4):1038–1065.

Kronenberg, A. K. and Shelton, G. L. (1980). Deformation microstructures in experimentally deformed Maryland diabase. *Journal of Structural Geology*, 2(3):341–353.

Lamb, S. (2006). Shear stresses on megathrusts: Implications for mountain building behind subduction zones. *Journal of Geo-*
575 *physical Research: Solid Earth*, 111(B7).

Li, D., McGuire, J. J., Liu, Y., and Hardebeck, J. L. (2018). Stress rotation across the cascadia megathrust requires a weak subduction plate boundary at seismogenic depths. *Earth and Planetary Science Letters*, 485:55–64.

Liou, J., Ho, C., and Yen, T. (1975). Petrology of some glaucophane schists and related rocks from taiwan. *Journal of Petrology*, 16(1):80–109.

Michel, S., Gualandi, A., and Avouac, J. P. (2019). Similar scaling laws for earthquakes and Cascadia slow-slip events. *Nature*, 574(7779):522–526.

Misch, P. (1969). Paracrystalline microboudinage of zoned grains and other criteria for synkinematic growth of metamorphic minerals. *American Journal of Science*, 267(1):43–63.

Muñoz-Montecinos, J., Angiboust, S., and Garcia-Casco, A. (2021). Blueschist-facies paleo-earthquakes in a serpentinite channel (Zagros suture, Iran) enlighten seismogenesis in Mariana-type subduction margins. *Earth and Planetary Science Letters*, 573:117135.

Muñoz-Montecinos, J. et al. (2023). Shattered veins elucidate brittle creep processes in the deep slow slip and tremor region. *Tectonics*, 42(4).

Nishimura, T., Matsuzawa, T., and Obara, K. (2013). Detection of short-term slow slip events along the Nankai Trough, southwest Japan, using GNSS data. *Journal of Geophysical Research: Solid Earth*, 118(6):3112–3125.

Nyman, M. W., Law, R. D., and Smelik, E. A. (1992). Cataclastic deformation mechanism for the development of core-mantle structures in amphibole. *Geology*, 20(5):455–458.

Okazaki, K. and Hirth, G. (2020). Deformation of mafic schists from subducted oceanic crust at high pressure and temperature conditions. *Tectonophysics*, 774:228217.

Ott, J. N., Condit, C. B., Schulte-Pelkum, V., Bernard, R., and Pec, M. (2024). Seismic Anisotropy of Mafic Blueschists: EBSD-Based Constraints From the Exhumed Rock Record. *Journal of Geophysical Research: Solid Earth*, 129(2).

Ozawa, S. (2017). Long-term slow slip events along the Nankai trough subduction zone after the 2011 Tohoku earthquake in Japan. *Earth, Planets and Space*, 69(1).

Park, Y. and Jung, H. (2022). Seismic velocity and anisotropy of glaucophane and epidote in experimentally deformed epidote blueschist and implications for seismic properties in warm subduction zones. *Earth and Planetary Science Letters*, 598:117822.

Park, Y., Jung, S., and Jung, H. (2020). Lattice preferred orientation and deformation microstructures of glaucophane and epidote in experimentally deformed epidote blueschist at high pressure. *Minerals*, 10(803).

Penney, C., Tavakoli, F., Saadat, A., Nankali, H. R., Sedighi, M., Khorrami, F., Sobouti, F., Rafi, Z., Copley, A., Jackson, J., and Priestley, K. (2017). Megathrust and accretionary wedge properties and behaviour in the Makran subduction zone. *Geophysical Journal International*, 209(3):1800–1830.

Philippot, P. and van Roermund, H. L. (1992). Deformation processes in eclogitic rocks: evidence for the rheological delamination of the oceanic crust in deeper levels of subduction zones. *Journal of Structural Geology*, 14(8-9):1059–1077.

Poirier, J.-P. (1985). *Dislocation creep models*. Cambridge Earth Science Series. Cambridge University Press.

Proctor, B. and Hirth, G. (2016). "ductile to brittle" transition in thermally stable antigorite gouge at mantle pressures. *Journal of Geophysical Research: Solid Earth*, 121(3):1652–1663.

Radiguet, M., Cotton, F., Vergnolle, M., Campillo, M., Walpersdorf, A., Cotte, N., and Kostoglodov, V. (2012). Slow slip events and strain accumulation in the Guerrero gap, Mexico. *Journal of Geophysical Research: Solid Earth*, 117(4):1–13.

Reynard, B., Gillet, P., and Willaime, C. (1989). Deformation mechanisms in naturally deformed glaucophanes; a tem and hrem study. *European Journal of Mineralogy*, 1(5):611–624.

615   Richter, B., Stünitz, H., and Heilbronner, R. (2018). The brittle-to-viscous transition in polycrystalline quartz: An experimental study. *Journal of Structural Geology*, 114(September 2017):1–21.

Rousset, B., Fu, Y., Bartlow, N., and Bürgmann, R. (2019). Week-Long and Year-Long Slow Slip and Tectonic Tremor Episodes on the South Central Alaska Megathrust. *Journal of Geophysical Research: Solid Earth*, 124(12):13392–13403.

Rubie, D. C. (1983). Reaction-enhanced ductility: The role of solid-solid univariant reactions in deformation of the crust and
620   mantle. *Tectonophysics*, 96(3-4):331–352.

Schmidt, D. A. and Gao, H. (2010). Source parameters and time-dependent slip distributions of slow slip events on the Cascadia subduction zone from 1998 to 2008. *Journal of Geophysical Research: Solid Earth*, 115(4):1–13.

Schmidt, W. L. and Platt, J. P. (2022). Stress, microstructure, and deformation mechanisms during subduction underplating at the depth of tremor and slow slip, franciscan complex, northern california. *Journal of Structural Geology*, 154:104469.

625   Shaocheng, J., Salisbury, M. H., and Hanmer, S. (1993). Petrofabric, P-wave anisotropy and seismic reflectivity of high-grade tectonites. *Tectonophysics*, 222(2):195–226.

Sibson, R. H. (2017). Tensile overpressure compartments on low-angle thrust faults. *Earth, Planets and Space*, 69:1–15.

Speciale, P., Behr, W. M., Hirth, G., and Tokle, L. (2020). Rates of olivine grain growth during dynamic recrystallization and postdeformation annealing. *Journal of Geophysical Research: Solid Earth*, 125(11):e2020JB020415.

630   Stipp, M. and Kunze, K. (2008). Dynamic recrystallization near the brittle-plastic transition in naturally and experimentally deformed quartz aggregates. *Tectonophysics*, 448(1-4):77–97.

Sun, T., Saffer, D., and Ellis, S. (2020). Mechanical and hydrological effects of seamount subduction on megathrust stress and slip. *Nature Geoscience*, 13(3):249–255.

Takagi, R., Uchida, N., and Obara, K. (2019). Along-Strike Variation and Migration of Long-Term Slow Slip Events in the Western
635   Nankai Subduction Zone, Japan. *Journal of Geophysical Research: Solid Earth*, 124(4):3853–3880.

Tatham, D. J., Lloyd, G. E., Butler, R. W., and Casey, M. (2008). Amphibole and lower crustal seismic properties. *Earth and Planetary Science Letters*, 267(1-2):118–128.

Thomas, A. M., Beroza, G. C., and Shelly, D. R. (2016). Constraints on the source parameters of low-frequency earthquakes on the san andreas fault. *Geophysical Research Letters*, 43(4):1464–1471.

640   Tokle, L. et al. (2023a). Diffusion creep of sodic amphibole-bearing blueschist limited by microboudinage. *Journal of Geophysical Research: Solid Earth*, 128(9).

Tokle, L., Hirth, G., and Behr, W. M. (2019). Flow laws and fabric transitions in wet quartzite. *Earth and Planetary Science Letters*, 505:152–161.

Tokle, L., Hirth, G., Liang, Y., Raterron, P., and Dygert, N. (2021). The Effect of Pressure and Mg-Content on Ilmenite Rheology:
645   Implications for Lunar Cumulate Mantle Overturn. *Journal of Geophysical Research: Planets*, 126(1):1–20.

Tokle, L., Hirth, G., and Stünitz, H. (2023b). The effect of muscovite on the microstructural evolution and rheology of quartzite in general shear. *Journal of Structural Geology*, 169.

Tullis, J. and Yund, R. (1992). *The brittle-ductile transition in feldspar aggregates: An experimental study*, volume 51 of *International geophysics*. Academic Press.

650   Tullis, J. and Yund, R. A. (1985). Dynamic recrystallization of feldspar: a mechanism for ductile shear zone formation. *Geology*, 13(4):238–241.

Tullis, J. and Yund, R. A. (1987). Transition from cataclastic flow to dislocation creep of feldspar: mechanisms and microstructures. *Geology*, 15(7):606–609.

Wang, K. and Bilek, S. L. (2011). Do subducting seamounts generate or stop large earthquakes? *Geology*, 39(9):819–822.

655   Warren, J. M. and Hirth, G. (2006). Grain size sensitive deformation mechanisms in naturally deformed peridotites. *Earth and Planetary Science Letters*, 248(1-2):438–450.

Zhang, J. and Green, H. W. (2007). Experimental investigation of eclogite rheology and its fabrics at high temperature and pressure. *Journal of Metamorphic Geology*, 25(2):97–115.